THE JOURNAL OF PHYSICAL CHEMISTRY C
A JOURNAL OF THE AMERICAN CHEMICAL SOCIETY

pubs.acs.org/JPCC Article

Ruddlesden–Popper Perovskite Alloys: Continuous and Discontinuous Tuning of the Electronic Structure

Published as part of The Journal of Physical Chemistry virtual special issue "Early-Career and Emerging Researchers in Physical Chemistry Volume 2".

Kameron R. Hansen,* Blake Romrell, C. Emma McClure, Michele Eggleston, Alex Berzansky, Jeffrey Wayjer Lin, Kelsey Garden, Luisa Whittaker-Brooks,* and John S. Colton*

Cite This: *J. Phys. Chem. C* 2023, 127, 9344–9353 Read Online

ABSTRACT: Alloying mixed ratios of elements into the halide perovskite (HP) structure has proven to be an effective method of tuning these materials' structural and electronic properties for photovoltaic and other optoelectronic applications. However, the standard spectroscopies used to characterize HP alloys such as absorption and photoluminescence are limited in their ability to detect disorder and phase segregation within the structure. Here, we characterize these properties in 2D HP alloys to a greater degree by using electroabsorption spectroscopy to study thin films with mixed-metal (Pb–Sn) and mixed-halide (Br–Cl and Br–I) compositions. The large spectral separation of band-edge states in 2D HPs allow us to detect a coexistence of elemental-rich domains within the Pb–Sn and Br–I alloys. Meanwhile, we find that the Br–Cl alloys exhibit sharper spectral features and a more uniform electroabsorption response indicative of an ordered structure, albeit still not as ordered as their pure Br and Cl counterparts. The band gap energies of the Br–Cl series ($PEA_2PbBr_xCl_{4-x}$) can be continuously tuned between 3.425 and 4.13 eV via the Br:Cl ratio, while the exciton binding energies can be tuned from 349 to 487 meV.

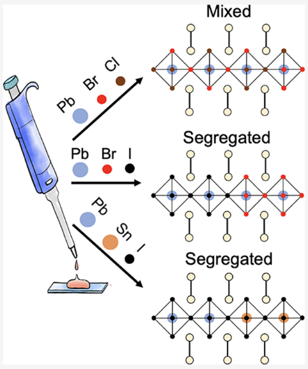

INTRODUCTION

Due to their high solar-conversion efficiencies, ideal band gap energies, and inexpensive processing, halide perovskites (HPs) offer exciting potential as photovoltaic materials that can help meet the world's rising energy demands. In so-called three-dimensional HPs, the lattice has a general formula of ABX_3, where the A-site is occupied by a cation (typically methylammonium, MA, or formamidinium, FA), the B-site is a metal atom (typically Pb^{2+} or Sn^{2+}), and the X-site is a halide atom (typically I^-, Br^-, or Cl^-). The metal and halide atoms form $[BX_6]^{4-}$ octahedral units that touch at the corners, either extending into three dimensions or potentially forming lower-dimensional structures that confine the charge carriers. Alloying different ratios of occupants within the A-, B-, and X-sites is an effective strategy to tune the optoelectronic properties and increase film stability. Generally speaking, the highest-performing HP devices have mixed-halide compositions. For example, the "kitchen sink" composition $Cs_zFA_xMA_{1-x-z}PbBr_yI_{3-y}$ routinely outperforms the prototypical $MAPbI_3$ composition,[1] and considerable research efforts have also been devoted to studying mixed B-site alloys as well, such as Pb–Sn alloys.[2–6]

Upon synthesis of a given alloy composition, there are typically two central questions underscoring the characterization of the product material: first, to what extent are the mixed elements homogeneously distributed throughout the structure, and second, what degree of optoelectronic tunability is offered by the mixing of these elements into the structure. Naturally, the two questions are related given that the physical structure dictates the electronic band structure and all optoelectronic properties. After a decade of research efforts investigating these questions for specific 3D HP alloy compositions, it is understood that the absorption onset (optical gap) of mixed Br–I alloys can be tuned via the Br:I ratio; however, segregation into Br-rich and I-rich domains can often occur under modest exposure to light.[7−9] On the other hand, Br–Cl alloys form much more stable structures and exhibit optoelectronic properties that vary monotonically with the Br:Cl ratio.[10] The Pb–Sn alloys also exhibit tunable band gap energies (E_g)[2,3,11] and potentially tunable exciton binding energies (E_b) and reduced effective masses as well (μ).[4] However, Pb–Sn alloys are difficult to characterize due to their broad spectral features and the rapid oxidation of $Sn^{2+} \rightarrow Sn^{4+}$.[12]

Received: February 24, 2023
Revised: April 16, 2023
Published: May 3, 2023

https://doi.org/10.1021/acs.jpcc.3c01294
J. Phys. Chem. C 2023, 127, 9344–9353

For each of these alloyed compositions, the primary evidence for the tunability of the optoelectronic properties has come by way of photoluminescence (PL) and absorption spectroscopies. Typically, the PL peak energy or absorption onset is measured for several E_1:E_2 ratios where E_1 and E_2 represent the two alloyed elements, and the PL or exciton absorption peaks between the 1:0 and 0:1 endpoints are taken as evidence of alloyed crystal phases.[11,13−16] While this approach is generally valid, the information gained from PL and absorption spectroscopies on the bulk material is limited. For example, a crystal with a coexistence of E_1-rich and E_2-rich domains may have overlapping absorption features that, when summed together in a bulk measurement, are easily mistaken for a single crystal phase. Likewise, charge transfer between E_1-rich and E_2-rich regions can occur,[17] potentially resulting in optical signals based on the lowest-lying energy state. As a result, these experiments can leave open the possibility for higher-E_g crystal phases to be present within the sample and go undetected. Furthermore, within the width of the material's absorption features, there is a continuum of possible alloyed phases with slightly different E_1:E_2 ratios that such experiments are unable to distinguish.

To navigate these challenges, our strategy in this article is to study two-dimensional HP alloys via low-temperature electroabsorption (EA) spectroscopy. In 2D HPs, confinement effects enhance E_b by an order of magnitude relative to their 3D counterparts, which allows band-edge spectral features to be resolved by EA. The 2D HP thin films are cooled to 15 K to reduce the width of the absorption features, and EA is used to probe the critical points in the electronic structure. Under these conditions, it is possible to detect nonuniformities that would otherwise go unnoticed in linear absorption experiments at room temperature or for 3D HPs where the broadening factor Γ is large and E_b is low.

Two-dimensional HPs are analogous to their 3D counterparts in that the band structure originates from the same $[BX_6]^{4-}$ octahedral unit but with bulky A-site cations separating the octahedra into 2D sheets, which create large confinement effects.[18,19] The 2D HP "Ruddlesden−Popper" crystal structure (shown in Figure 1a) has a general formula A_2BX_4, where the A-site cation typically takes the form of $C_6H_5CH_2CH_2NH_3^+$ (phenethylammonium, PEA) or $CH_3(CH_2)_3NH_3^+$ (butylammonium, BA). The mismatch in band alignment between the organic/inorganic layers confines electrons and holes within the inorganic layer, while the mismatch in dielectric constants also results in an image charge effect (dielectric confinement).[20,21]

While alloying in 3D HPs has been extensively studied, far less is known about alloying in 2D HPs, which are important materials in their own respect as they are effective capping layers for 3D HP solar cells and have potential for a wide range of light-absorbing and light-emitting applications.[18,22−24] Alloying the B-site and X-site have been popular strategies when making 2D HP devices;[25] however, fundamental characterization of the elemental homogeneity and optical properties are lacking. Recently, a handful of studies have begun to fill this knowledge gap. A 2021 article by Cho et al. compared light-induced Br−I segregation in 3D HPs ($MAPbBr_{1.5}I_{1.5}$) and 2D HPs ($PEA_2PbBr_2I_2$) and found much lower segregation in the 2D case.[9] However, the overall halide segregation and the film composition were not quantified. A subsequent study by Wright et al. targeted $PEA_2PbBr_xI_{4-x}$ alloys with x = [0, 1, 2, 3, 4] and found significant halide segregation for all Br:I ratios.[26] By contrast, the Br:Cl alloys remain largely unstudied. Finally, there have been a handful of studies focused on mixed-metal Ruddlesden−Popper structures with varying ratios of Pb:Sn; however, the spatial heterogeneity of the Pb−Sn atoms remains an open question as these studies have focused on other questions such as defect photoluminescence,[27] solar cell efficiency,[28−30] etc. Theoretical studies have discussed the benefits of Br−I and Pb−Sn alloying in 2D HPs[31,32] using models that assume homogeneous distributions of the elements, yet it remains unclear whether or not such homogeneous structures will naturally crystalize.

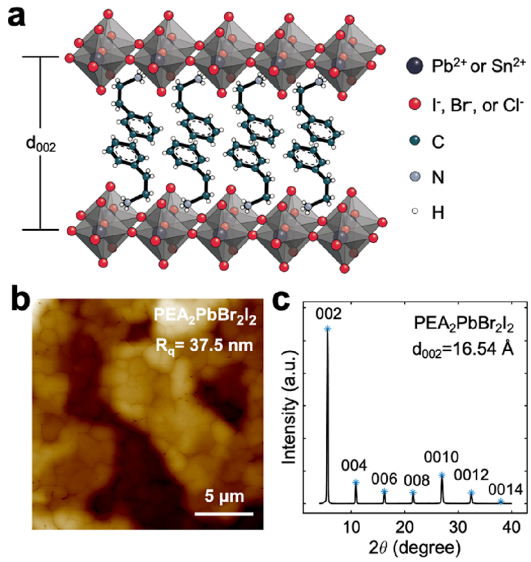

Figure 1. (a) Schematic of the PEA_2BX_4 crystal structure. The organic cation PEA ($C_6H_5CH_2CH_2NH_3^+$) separates the inorganic octahedra ($[BX_6]^{4-}$) into two-dimensional sheets. (b) AFM image of a $PEA_2PbBr_2I_2$ thin film showing ∼2 μm grains and an RMS surface roughness (R_q) of 37.5 nm. (c) Representative XRD pattern of the same $PEA_2PbBr_2I_2$ thin film where diffraction from the $\{00l\}$ family of crystallographic planes indicating that the 2D HP structure has its c axis predominantly oriented perpendicular to the substrate.

This study aims to quantify disorder and phase segregation in mixed-halide (Br−I and Br−Cl) and mixed-metal (Pb−Sn) 2D HP thin films using primarily X-ray diffraction (XRD) and low-temperature electroabsorption (EA) spectroscopy. We find that the Br−Cl alloys have sharp spectral features with energies that can be continuously tuned via the Br:Cl ratio. This is in contrast to the Pb−Sn alloys and Br−I alloys where the spectral features are broader and more numerous, indicating a coexistence of elemental-rich domains within the thin film.

■ METHODS

Thin Film Fabrication and Structural Characterization. 2D HP thin films were fabricated by dissolving metal−iodide salts ($PbCl_2$, $SnCl_2$, $PbBr_2$, $SnBr_2$, PbI_2, and SnI_2) with stoichiometric ratios of a phenethylamine salt (PEA−Cl, PEA−Br, and PEA−I) in a 4:1 DMF:DMSO solvent mixture. For example, to produce a 0.3 M precursor solution of $PEA_2PbBr_2I_2$, 55 mg of $PbBr_2$, 69 mg of PbI_2, 61 mg of PEABr, and 75 mg of PEAI were mixed in 1 mL of the 4:1 DMF:DMSO solvent mixture. To spin-coat a thin film, substrates were cleaned via sonication in soapy water, distilled water, acetone, and isopropanol and then plasma-cleaned under vacuum. Thin films were spin-coated onto soda lime

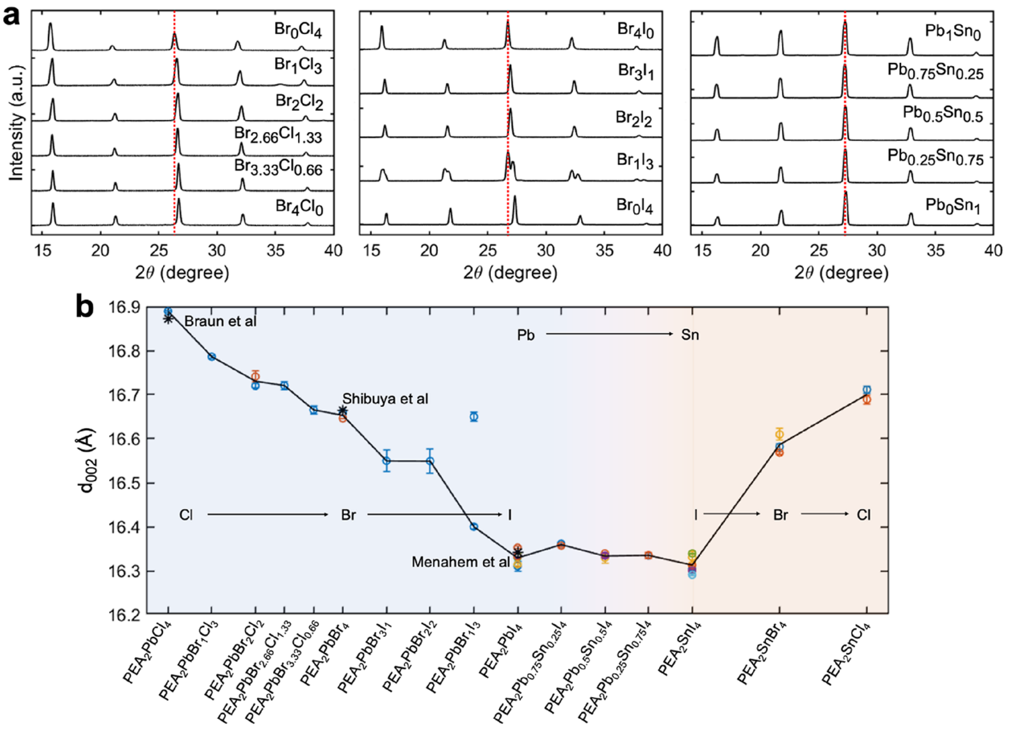

Figure 2. (a) XRD patterns for the $PEA_2PbBr_xCl_{4-x}$ series (left), $PEA_2PbBr_xI_{4-x}$ series (middle), and $PEA_2Pb_xSn_{1-x}I_4$ series (right). In order to compare the peak positions, the intensities have been normalized, and the horizontal axis is zoomed in on $14 \leq 2\theta \leq 40$, which corresponds to diffraction from the $\{00l\}$ planes, where $6 \leq l \leq 14$. (b) The interlayer distance (d_{002}) for various PEA_2BX_4 compositions which was found by applying Bragg's law to three highest-order peaks ($l = 10, 12, 14$). The error bars indicate the standard deviation for these three points. The black asterisks correspond to single-crystal XRD values reported by Braun et al. for PEA_2PbCl_4,[40] Shibuya et al. for PEA_2PbBr_4,[36] and Menahem et al. for PEA_2PbI_4.[37] Multiple open circles for the same composition correspond to thin films made on different days from different precursor solutions.

glass for XRD measurements and onto quartz substrates with ∼120 nm thick interdigitated gold electrodes for absorption and EA measurements. The precursor solution was pipetted onto the substrate and spun at 4000 rpm for 30 s, at which point the substrate was placed on a 100 °C hotplate for 10 min. We found it necessary to use a low precursor solution molarity (0.05−0.3 M) in order to keep the film's peak optical density between 0.5 and 2 OD for the absorption and EA measurements. An X-ray diffractometer (Bruker D8 Discover) with Cu K_α radiation (1.5406 Å) was used to collect the X-ray diffraction (XRD) patterns. The AFM images were collected on a Bruker Dimension Icon atomic force microscope in tapping mode.

Optical Spectroscopies. Electroabsorption was collected in transmission mode according to methods previously reported.[33,34] The small distance between the opposing electrode fingers (d = 50 μm) allows for the generation of large electric fields (62−156 kV/cm) using voltages in the range of 280−700 V. Thin copper wires were soldered to the opposing electrode stripes, and samples were mounted in a cryostat for low-temperature measurements. Optical absorption was collected using a Xe lamp spectrally filtered through a 0.25 m f/3.5 monochromator with a 1.5 nm spectral resolution, focused onto the sample, and then refocused onto a silicon photodiode detector. The RMS value of the photodiode's signal was demodulated with a Stanford Research Systems SR810 or SR830 lock-in amplifier operating in current mode. The difference in absorbance with and without a static electric field (ΔA) was calculated from the normalized electrotransmission spectrum $\Delta T/T$, where T and ΔT were collected as independent wavelength scans. For T and T_0 (transmission of sample on IDE substrate and transmission of blank IDE substrate, respectively), the signal was detected at the first harmonic of the mechanical chopper's frequency (∼330 Hz), whereas the ΔT signal was lock-in detected at the first harmonic of the modulating signal, $V_{AC}(t)$. The absorbance was calculated as $A = \log_{10}(T_0/T)$. The EA response is then given by

$$\Delta A = -\log_{10}\left(1 + \frac{\Delta T}{T}\right) \tag{1}$$

Typically, an instrumental correction factor is needed in eq 1.[34,35] However, in our case, the modulating voltage is a pulse wave with a waveform similar to that of the mechanical chopper, and we measured this factor to be 1 ± 0.01, i.e., no correction is needed.

■ RESULTS AND DISCUSSION

Synthesis and Structural Characterization. To investigate the optical properties of mixed-halide (Br−Cl and Br−I) and mixed-metal (Pb−Sn) 2D HPs, we fabricated thin films to target the following compositions: PEA_2PbCl_4, $PEA_2PbBr_1Cl_3$, $PEA_2PbBr_2Cl_2$, $PEA_2PbBr_{2.66}Cl_{1.33}$, $PEA_2PbBr_{3.33}Cl_{0.66}$, PEA_2PbBr_4, $PEA_2PbBr_3I_1$, $PEA_2PbBr_2I_2$, $PEA_2PbBr_1I_3$, PEA_2PbI_4, $PEA_2Pb_{0.75}Sn_{0.25}I_4$, $PEA_2Pb_{0.5}Sn_{0.5}I_4$, $PEA_2Pb_{0.25}Sn_{0.75}I_4$, PEA_2SnI_4, PEA_2SnBr_4, and PEA_2SnCl_4. These compositions were chosen to provide three alloy series, namely, $PEA_2Pb(Br_xCl_{1-x})_4$ with x = 0, 16.5, 33.25, 50, 75, and 100%; $PEA_2Pb(Br_xI_{1-x})_4$ with x = 0, 25, 50, 75, and 100%; and $PEA_2Pb_xSn_{1-x}I_4$ with x = 0, 25, 50, 75, and 100%; with PEA_2SnBr_4 and PEA_2SnCl_4 additionally being included in order to give an indication of what is likely to be achievable with halide substitution and alloying in Sn compounds. The labels represent the stoichiometry of the elements added to the precursor solution and not necessarily the stoichiometry of the crystallized film that formed upon spin-coating the precursor solution. The Ruddlesden−Popper structure was verified for each of the targeted compositions by XRD. The surface morphology of the thin films was investigated using atomic force microscopy (AFM). The AFM image of the $PEA_2PbBr_2I_2$ composition is shown in Figure 1b, which displays a grain size of ∼2 um and RMS surface roughness (R_q) of 37.5 nm; the AFM images for several other compositions are presented in Figure S1.

To probe the atomic structure within the grains, powder XRD patterns were collected for each composition. A representative XRD pattern is shown in Figure 1c for the $PEA_2PbBr_2I_2$ composition, where the peaks at regular 2θ intervals correspond to diffraction from the $\{00l\}$ family of crystallographic planes. Using Bragg's law, these 2θ angles can be converted to an interlayer thickness (labeled "d_{002}" in Figure 1a); we found d_{002} = 16.54 Å for $PEA_2PbBr_2I_2$, which is centered between the reported values of PEA_2PbBr_4 and PEA_2PbI_4 in single-crystal XRD studies.[36,37] The lack of additional XRD peaks beyond those originating from the $\{00l\}$ planes indicates a pure Ruddlesden−Popper structure with layers predominately oriented parallel to the substrate.[38] XRD patterns for all the samples are found in Supplementary Information Figure S2. As shown in Figure S3 and Figure S4, the absorption spectrum and XRD patterns of the spin-coated alloy films in this study are strikingly similar to the blade-coated films in ref5 and the laser-evaporated films in ref26. These similarities among the spin-coated, blade-coated, and laser-evaporated films suggest that the properties of the alloyed films depend on the stoichiometry of the precursor elements more than the processing technique. However, it remains a possibility that novel synthetic approaches can overcome these tendencies to produce high-quality films regardless of the composition. This study focuses exclusively on the properties of the spin-coated thin films.

Since the atomic radius of the X-site atom increases moving from Cl (1.00 Å) to Br (1.15 Å) to I (1.40 Å) and the B-site atom's radius decreases moving from Pb (1.8 Å) to Sn (1.4 Å),[39] in accordance with Vegard's law, the degree of alloying within a given structure should be indicated to some extent by the d_{002} spacing determined from XRD. In Figure 2a, the XRD patterns of the alloyed compositions are plotted for the mixed Br−Cl (left), Br−I (middle), and Pb−Sn (right) thin films. The horizontal axis in the figure is zoomed in on the higher-order diffraction peaks (l = 6, 8, 10, 12, 14), and the intensities are normalized for easy visual comparison. The dotted red line intersects marks the $l = 10$ peak position of the pure PEA_2PbCl_4 (left), PEA_2PbBr_4 (middle), and PEA_2PbI_4 (right) structures. As is clear to the eye, the 2θ position of this peak in the left figure gradually shifts to higher angles as bromine is incorporated into the PEA_2PbCl_4 structure. A similar trend is observed in the middle figure as iodine is incorporated into PEA_2PbBr_4. However, for the Br:I = 3:1 sample, a double peak is observed, indicating two phases, with the 2θ positions matching those of the PEA_2PbBr_4 and PEA_2PbI_4 structures. Meanwhile, the peaks in the Pb−Sn series (Figure 2a, right) are roughly aligned for all ratios of Pb:Sn, even for the PEA_2PbI_4 and PEA_2SnI_4 endpoints. To quantify these peak positions, the center positions were obtained via Gaussian fits and converted to a d_{002} distance using Bragg's law. These d_{002} values are plotted in Figure 2b, where each datapoint was calculated by averaging the three highest-order $\{00l\}$ diffraction peaks (l = 10, 12, and 14) and the error bars indicate the standard deviation for these three points.

Our measurements on thin films (marked by open circles in Figure 2b) are in agreement with literature values taken from single-crystal XRD studies (asterisks),[40,36,37] and we observe a clear trend of d_{002} decreasing from Cl (16.90 Å) to Br (16.67 Å) to I (16.31 Å). Interestingly, this is opposite the trend one would expect from a simple atomic radius picture, seeing as the radius increases moving from Cl → Br → I. It is also opposite the trend one would expect from a bond strength picture since the bond strength decreases moving from Cl → Br → I according to the halide atom's electronegativity, suggesting tighter atomic packing in the Cl case. Indeed, for these reasons, the three-dimensional ABX_3 lattice expands moving from Cl → Br → I.[41,42] However, the reverse trend is observed here for the two-dimensional A_2BX_4 structures consistent with the literature; this is not clearly understood but is likely due to specifics of the amine−halide bond and van der Waals interactions between PEA molecules that are beyond the scope of this study.

The d_{002} values of the Br−Cl and Br−I alloys follow a fairly linear trend in Figure 2b, which provides strong evidence that the halides are being successfully alloyed into the X-site. Alloying within the B-site is less clear from the XRD data due to the similarity of the d_{002} values for the PEA_2PbI_4 and PEA_2SnI_4 endpoints. The uncertainty in the exact crystal structure and the measurement uncertainty in d_{002} leave several questions unanswered, such as the homogeneity of the crystal phases within the thin film and the homogeneity of the optoelectronic properties. One might suspect that the former could be determined through analysis of the XRD peak widths since the diffraction peak widths relate to structural disorder; however, we found the XRD peak widths to be primarily determined by instrumental uncertainty (see Figure S5). To answer these questions, we instead turn to absorption and EA spectroscopies.

Absorption and EA Spectroscopy. The central aim of this study is to probe the optoelectronic properties of HP alloys more thoroughly than XRD or the traditional spectroscopies (absorption, transient absorption, photoluminescence, etc.) of past studies. Electroabsorption, i.e., the difference in a material's absorption spectrum with and without an applied electric field, is effective at measuring the properties that we seek to characterize such as disorder and phase segregation. The EA signal is measured as a normalized difference signal either in transmission $\Delta T/T$ or reflection $\Delta R/R$ geometries, where broad backgrounds and optical scattering effects are eliminated.[43]

As demonstrated in previous studies by our group, the low-temperature EA spectrum of 2D HPs provides trustworthy measurements of the 1s exciton (E_{1s}) and band gap (E_g) energies through zero-crossing points in the EA spectrum.[34,44,45] These E_{1s} and E_g points are marked by an open circle and asterisks, respectively, in the schematic EA response shown in Figure 3a. Here, the solid gray line represents the normal absorption spectrum of a typical excitonic 2D semiconductor, while the dotted red line represents the absorption in the presence of an applied electric field, F. The difference between these spectra, i.e., the EA spectrum $\Delta A = A(F > 0) - A(F = 0)$, is shown in Figure 3b. Electric fields have two primary effects on the absorption. First, below the

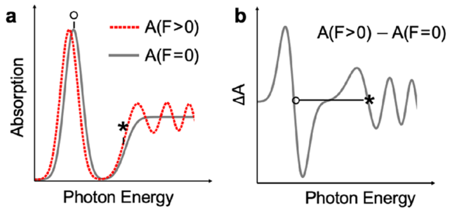

Figure 3. (a) Schematic of a typical absorption spectrum (solid gray) and electric field-shifted absorption spectrum (dotted red) for a typical 2D excitonic semiconductor. The application of an electric field redshifts the exciton peak due to the Stark effect, while Airy-function-like oscillations occur at the interband transitions as a result of the Franz−Keldysh effect. The difference between the two spectra produces (b) the electroabsorption spectrum where the zero-crossings of the exciton (circle) and interband (asterisks) features mark the E_{1s} and E_g, respectively.

band gap, the Stark effect redshifts and broadens the exciton peak, producing first- and second-derivative-type lineshapes in the EA signal, respectively. If the lineshape is purely first-derivative, then the zero-crossing of this feature precisely marks E_{1s} as is the case for the example in Figure 3. However, if there is a significant second-derivative component as is often the case for disordered films, then E_{1s} is more accurately determined by the exciton peak in the linear absorption, marked by an open circle. The second electric field effect is the Franz−Keldysh (FK) effect, which occurs at energies near and above the band gap. At these energies, the FK effect produces Airy function-like oscillations in the interband absorption. Experimentally, only the first of these FK oscillations is observed in HP systems. The FK nature of this feature can be unambiguously identified through the electric field dependence of the feature's amplitude and width, and the zero-crossing of the FK feature accurately marks the E_g.[34] The exciton binding energy can then be straightforwardly determined as per its definition, $E_b = E_g - E_{1s}$.

EA Response of the Non-Alloyed Compositions. In Figure 4, the absorption and EA of the PEA_2BX_4 structures are shown for BX_4 = SnI_4, $Pb_{0.5}Sn_{0.5}I_4$, PbI_4, $PbBr_2I_2$, $PbBr_4$, $PbBr_2Cl_2$, and $PbCl_4$. The non-alloyed 2D HP compositions have been reported previously by our group,[34,44,46] but we repeat those results here to provide context for the results on alloyed structures. PEA_2SnI_4, PEA_2PbI_4, PEA_2PbBr_4, and PEA_2PbCl_4 all have similar absorption and EA lineshapes that resemble the schematic in Figure 3, and this allows for unambiguous assignments of E_{1s} (open circle) and E_g (asterisk) according to the established EA theory.[34] The length of the solid line represents the exciton binding energy, $E_b = E_g - E_{1s}$. The Stark and FK features are qualitatively similar in all of these compounds but displaced in energy as the band gap and exciton binding energy both increase moving from PEA_2SnI_4 → PEA_2PbI_4 → PEA_2PbBr_4 → PEA_2PbCl_4. The spectral features are particularly sharp for the three lead compositions, where the full width at half maximum (Γ) is less than 40 meV and multiple distinct exciton peaks are resolved, and these are marked by vertical red lines in Figure 4. In line with recent findings,[47,48] we interpret this multiplicity of exciton peaks to originate from distinct couplings with the lattice. Each excitonic peak Stark-shifts and produces multiple derivative-like oscillations in the below-gap EA signal. The absorption and EA features of PEA_2SnI_4 are broader by comparison due to more disorder within the film.[44]

EA Response of the Alloyed Compositions. By contrast, the absorption and EA of the alloyed compositions ($PEA_2Pb_{0.5}Sn_{0.5}I_4$, $PEA_2PbBr_2I_2$, and $PEA_2PbBr_2Cl_2$ in Figure 4) are less reminiscent of the prototypical EA response of 2D HPs. Instead, the EA signals show many features spread across a wide energy range. We take the multiplicity of EA features to represent a multiplicity of crystal phases within the thin film. One such composition that clearly falls into this category of having multiple distinct crystal phases is $PEA_2Pb_{0.5}Sn_{0.5}I_4$. Two sets of Stark and FK features are resolved in its EA spectrum

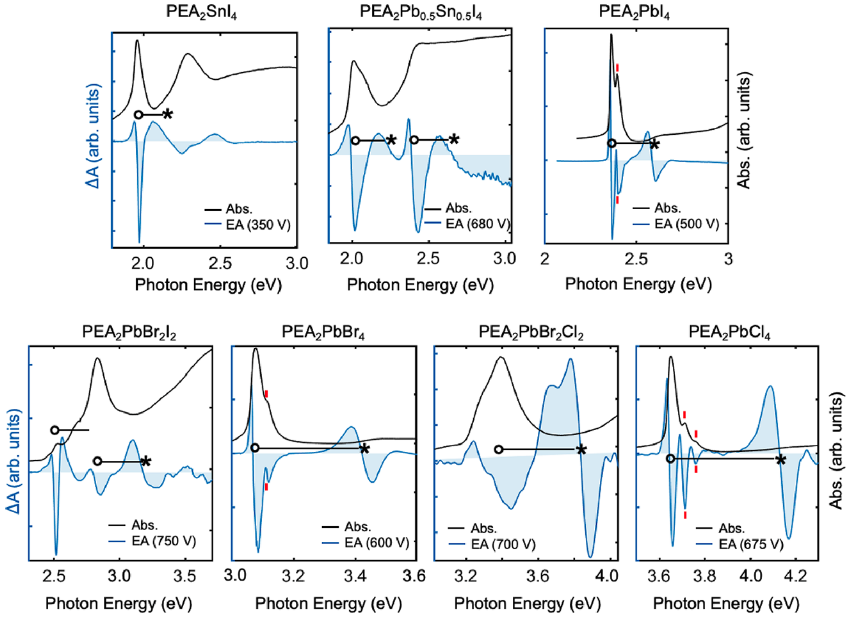

Figure 4. Double *y*-axis plots showing the electroabsorption spectrum (blue, left-hand *y* axis) and absorption spectrum (black, right-hand *y* axis) for several 2D HP compositions: PEA_2SnI_4, $PEA_2Pb_{0.5}Sn_{0.5}I_4$, PEA_2PbI_4, $PEA_2PbBr_2I_2$, PEA_2PbBr_4, $PEA_2PbBr_2Cl_2$, and PEA_2PbCl_4. The open circles mark E_{1s} (taken from the lowest-energy exciton absorption peak), while the asterisks mark the E_g (taken from the zero-crossing of the Franz-Keldysh feature in the EA spectrum).

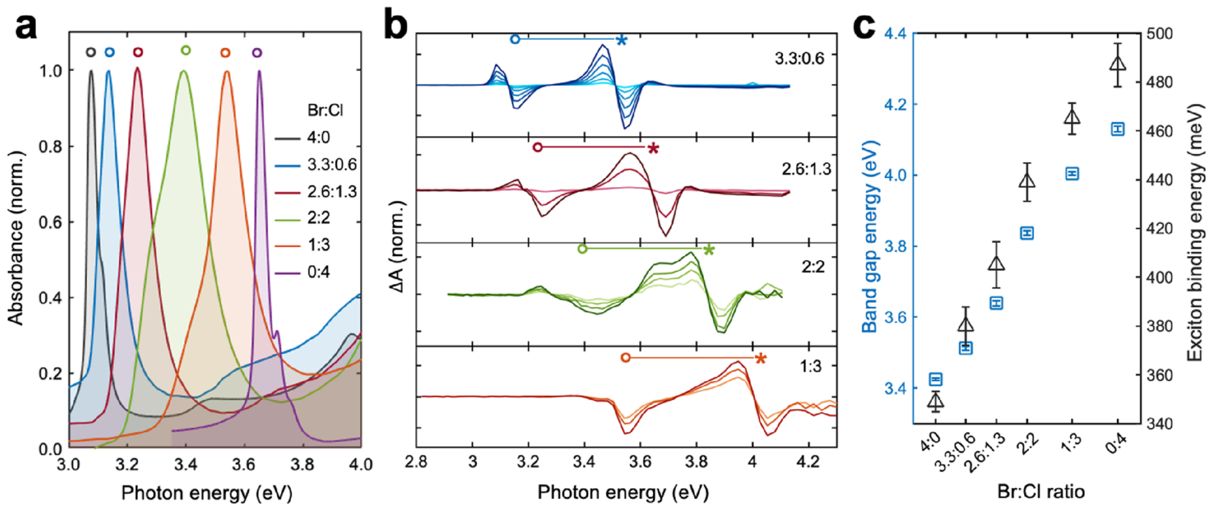

Figure 5. (a) Low temperature (15 K) absorbance spectra of $PEA_2PbBr_xCl_{4-x}$ thin films with Br:Cl ratios of 4:0, 3.33:0.66, 2.66:1.33, 2:2, 1:3, and 0:4. The alloyed compositions have broader exciton peaks than the non-alloyed compositions due to more static disorder within the thin film. (b) Low-temperature (15 K) EA spectra of the alloyed films. The band gap E_g is marked by an asterisk, while E_{1s} is marked by an open circle. The separation between the two, $E_g - E_{1s}$, is the exciton binding energy E_b. (c) Values of E_g and E_b as a function of the Br:Cl ratio.

(see Figure 4)—one pair that is close to the E_{1s} and E_g points of PEA_2SnI_4 near 2 eV and the other that is close to the E_{1s} and E_g points of PEA_2PbI_4 near 2.5 eV. The specific result for $PEA_2Pb_{0.5}Sn_{0.5}I_4$ is thus nearly a linear combination of the PEA_2SnI_4 and PEA_2PbI_4 EA spectra but does have some differences. The first important difference is that the E_{1s} and E_g points in the PEA_2SnI_4 region of the alloy film are ~50 meV higher in energy than those in PEA_2SnI_4, which suggests that a small fraction of Pb is alloyed into the Sn-rich domains. Moreover, the exciton's EA lineshape is more first-derivative-like and also appears to have a larger exciton binding energy than pure PEA_2SnI_4, and these are also both strong indicators of partial Pb content. Moving to higher energies, the close matching of the second E_{1s} point (2.389 eV) with that of PEA_2PbI_4 (2.364 eV) demonstrates that the Pb-rich regions of the alloyed film have very little, if any, Sn incorporated into the structure.

Low temperature absorption and EA spectra were also acquired for the $PEA_2Pb_{0.25}Sn_{0.75}I_4$ and $PEA_2Pb_{0.75}Sn_{0.25}I_4$ compositions (see Figure S6). Similar to $PEA_2Pb_{0.5}Sn_{0.5}I_4$, the EA signal for these compositions can be accurately described as a superposition of EA responses from distinct Sn-rich domains and Pb-rich domains. As the Pb fraction increases from 0 → 0.25 → 0.5 → 0.75, the E_{1s} point of the Sn-rich domain blueshifts from 1.962 eV → 2.005 eV → 2.01 eV → 2.09 eV, which again demonstrates that some lead is being alloyed into the Sn-rich domains.

Turning to the Br−I alloy, the EA spectrum of $PEA_2PbBr_2I_2$ in Figure 4 also reveals a coexistence of distinct crystal phases within the thin film. Among the overlapping absorption features, one exciton peak near 2.84 eV stands out as having the strongest absorption strength, and we pair this with a large interband FK feature centered at 3.179 eV. The difference, 339 meV, is the exciton binding energy and, as expected, falls between the E_b values of PEA_2PbI_4 (222 meV) and PEA_2PbBr_4 (349 eV). We deduce that this crystal phase is the most prevalent phase within the thin film and mostly Br in composition, as evidenced by the large absorption strength and the high band gap energy, respectively.

Unlike the other alloys, the EA of $PEA_2PbBr_2Cl_2$ somewhat resembles the prototypical EA response of 2D HPs, with a derivative-like Stark feature near 3.4 eV and an FK feature near 3.8 eV. The lack of additional features demonstrates that the electronic properties of the Br−Cl alloy are more homogeneous than the Pb−Sn and Br−I alloys, but still, the broadness of the features indicates some inhomogeneity in the film. Indeed, the exciton absorption exhibits a double peak, which we fit to a sum of two hyperbolic secants (shown in Figure S7) to extract excitonic peak energies of 3.286 and 3.398 eV for two separate crystal phases, with the higher energy peak being dominant. The small ~110 meV separation shows that the Br:Cl ratio only differs slightly between the two phases. These exciton energies are both close to the average of E_{1s} for PEA_2PbBr_4 (3.076 eV) and PEA_2PbCl_4 (3.643 eV), which indicates that the Br:Cl ratio for each phase is close to the 1:1 ratio of the precursor solution. Similarly, the left-hand side of the FK feature also displays a double peak. The presence of a second FK feature also argues for the presence of two distinct crystal phases with slightly differing Br:Cl ratios. The lower energy FK oscillation is not fully resolvable due to interaction with the dominant higher-energy FK oscillation, but the higher-energy FK oscillation has a zero crossing at 3.837 eV, which we then pair with the dominant, higher-energy exciton peak at 3.398 eV to deduce a binding energy of E_b = 439 meV. We note that the existence of two phases in this material could not have been deduced through XRD, presumably because the crystal structures are quite similar and cannot be detected within the XRD instrument resolution, which underscores the importance of using low-temperature EA as a tool in this manner.

These various observations of the $PEA_2PbBr_2Cl_2$ alloy motivated the hypothesis that the E_{1s} and E_g points could be finely tuned between the PEA_2PbBr_4 and PEA_2PbCl_4 endpoints by changing the Br:Cl ratio, and this question is tested in the following section.

Continuous Tunability of the $PEA_2PbBr_xCl_{4-x}$ Series. To test whether the optoelectronic properties of the Br−Cl alloys can be precisely tuned via the ratio of Br:Cl, additional absorbance and EA spectra were acquired for thin films with

Br:Cl ratios of 3.33:0.66, 2.66:1.33, and 1:3. These spectra are plotted in Figure 5 alongside the previously discussed Br:Cl ratios of 4:0, 2:2, and 0:4. As shown in Figure 5a, the exciton absorption monotonically blueshifts with increasing Cl concentration, and so does the position of the FK feature in the EA (Figure 5b) as well as their separation, which is the exciton binding energy. In two-dimensional semiconductors, E_g and E_b are correlated since both strongly depend on the polarizability (or dielectric constant) of the semiconducting layer,[49] and a strong linear correlation is observed here in accordance with a larger trend that we observed in a complementary study.[46] The values of E_b and E_g for this alloy series are listed in Table 1 and plotted as a function of the Br:Cl ratio in Figure 5c. As discussed in the introduction, low-temperature EA allows for far more precise measurements of the one-electron band gap E_g than traditional spectroscopies; thus, the results in Figure 5 are among the clearest evidence of E_g and E_b tunability in HP alloys to-date.

Table 1. E_{1s}, E_g, and E_b Values for the $PEA_2PbBr_xCl_{4-x}$ Series

composition	E_g (eV)	E_b (meV)
PEA_2PbBr_4	3.425 ± 0.003	349 ± 4
$PEA_2PbBr_{3.3}Cl_{0.6}$	3.512 ± 0.006	380 ± 8
$PEA_2PbBr_{2.6}Cl_{1.3}$	3.639 ± 0.008	405 ± 9
$PEA_2PbBr_2Cl_2$	3.837 ± 0.006	439 ± 8
$PEA_2PbBr_1Cl_3$	4.005 ± 0.005	465 ± 6
PEA_2PbCl_4	4.130 ± 0.008	487 ± 9

Measurements of Disorder. While the Br−Cl alloys have surprisingly sharp spectral features, the features are still nonetheless broader than those of the non-alloyed compositions, and it is clear that the alloyed films are more disordered. In the following, we quantify the disorder by analyzing the derivative lineshape of the exciton's EA signal and the width of the exciton absorption peak. As mentioned above, the lineshape of the exciton's EA spectrum (ΔA) takes the form of the first and second derivatives of the unperturbed absorbance (A), where the first derivative component relates to shifting and the second derivative relates to broadening. This can be written as follows:[34,50]

$$\Delta A = \gamma_1 \frac{dA}{dE} + \gamma_2 \frac{d^2A}{dE^2} \tag{2}$$

Here, γ_1 and γ_2 are factors that represent the strength of the quadratic and linear Stark effects, respectively, which also relate to the exciton's polarizability and dipole moment, respectively.[34] In particular, we consider the ratio of γ_2/γ_1 to be an effective measurement of the disorder from the exciton's perspective. This is because when asymmetry is introduced into the exciton's energy landscape (i.e., disorder), the polarizability (and hence γ_1) is reduced due to the localization of the electron and hole wavefunctions.[51] This effect is concomitant with an increase in the exciton's permanent dipole moment (and hence γ_2)[52] since the electron and hole wavefunctions in an asymmetric potential will shift in opposite directions from each other, leading to increased charge separation. Thus, to quantify the disorder, each of the EA spectra in Figure 4 plus the three additional alloy compositions from Figure 5 was fit to the first and second derivatives of the absorbance spectrum (i.e., eq 2) using linear regression, and the resulting γ_2/γ_1 ratios are reported in Table 2 alongside the FWHM of the excitonic absorption, Γ, which is another strong indicator of disorder.[53]

Table 2. Homogeneous Broadening of Excitonic Absorption (Γ) for 10 Compounds, along with the Ratio of Second- to First-Derivative Contributions to the Exciton's EA Lineshape (γ_2/γ_1)

	Γ (meV)	γ_2/γ_1 × 1000
PEA_2SnI_4	52	35.7
$PEA_2Pb_{0.5}Sn_{0.5}I_4$	80[a]	18.9[a]
PEA_2PbI_4	27	1.4
$PEA_2PbBr_2I_2$	204[b]	56.6[b]
PEA_2PbBr_4	37	6.1
$PEA_2PbBr_{3.33}Cl_{0.66}$	75	9.4
$PEA_2PbBr_{2.66}Cl_{1.33}$	101	35.1
$PEA_2PbBr_2Cl_2$	163[b]	63.3[b]
$PEA_2PbBr_1Cl_3$	122	74.0
PEA_2PbCl_4	35	8.7

[a] Lowest energy exciton peak near 2 eV. [b] Likely contains contributions from multiple crystal phases.

These two measures of disorder (γ_2/γ_1 and Γ) track quite closely with one another, as is shown in Figure 6. The alloyed films generally have larger Γ and γ_2/γ_1, indicating that these films have more static disorder in the form of point defects, grain boundaries, and lower overall film quality. The only exception to this trend is $PEA_2Pb_{0.5}Sn_{0.5}I_4$, where the γ_2/γ_1 is actually lower in the Pb:Sn alloy than in pure PEA_2SnI_4. This speaks to the intrinsically disordered nature of tin-based HPs, a subject that has been extensively investigated in previous articles.[44,54] By both metrics, Γ and γ_2/γ_1, the static disorder of the Br−Cl alloys is lowest when the Br concentration is high. The Γ and γ_2/γ_1 values rise as Cl is alloyed into the structure, reach a maximum at the $PEA_2PbBr_1Cl_3$ composition, and then drop significantly for pure PEA_2PbCl_4. Thus, we conclude that the mixed Br−Cl compositions crystallize into more ordered structures when the Br concentration outweighs the Cl concentration.

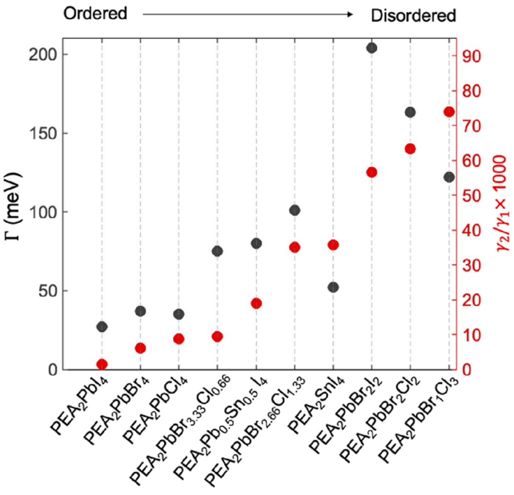

Figure 6. 2D HPs ranked approximately from most ordered to least ordered, as measured by Γ (black; left) and γ_2/γ_1 (red; right).

■ CONCLUSIONS

Since the rise of HP photovoltaics, 3D HP alloyed structures have been studied extensively both from structural and optoelectronic perspectives. In these studies, shifts in the PL peak energy and/or absorption onset are often taken as evidence that the electronic structure is tunable through the ratio of elements in the B- or X-sites. However, these experiments are ineffective in detecting optical features above the absorption onset or lowest-lying PL peak, and this allows for the possibility of higher-E_g crystal phases present within the sample to go undetected. In this study, we took advantage of the high exciton binding energy in 2D HPs and the sensitivity of EA spectroscopy to probe the electronic structure of 2D HP alloys with mixed B-site (Pb−Sn) and X-site (Br−Cl and Br−I) compositions. Despite having XRD patterns that suggest that the alloyed structure is continuously tunable, the low-temperature absorption and EA spectra reveal that in some cases, alloyed films can contain a coexistence of crystal phases with differing E_{1s} and E_g levels. In the Pb−Sn alloy, the crystal phases are drastically different, whereas for the Br−I and Br−Cl films, the differences between phases are much smaller. Additionally, by analyzing the absorption and EA lineshapes, we found that band edge states in the alloyed films are perturbed by disorder to a greater degree than in their non-alloyed counterparts. However, in the Br−Cl alloys, the amount of disorder is surprisingly low, especially when the Br concentration outweighs the Cl concentration. Optical measurements on the Br−Cl series reveal that E_g can be continuously tuned between 3.076 and 3.643 eV, while the exciton binding energy can be continuously tuned between 349 to 487 meV. Previous studies have shown that 2D HPs such as PEA_2PbBr_4 have excellent properties for UV photodetection,[55,56] and the results here demonstrate that the E_{1s}, E_g, and E_b can be precisely tuned for such applications. These findings advanced our understanding of disorder and optoelectronic tunability in 2D HP alloys, which may prove useful for a wide range of applications such as LEDs, capping layers in solar cells, photodetectors, and so forth.

■ ASSOCIATED CONTENT

Supporting Information

The Supporting Information is available free of charge at https://pubs.acs.org/doi/10.1021/acs.jpcc.3c01294.

> AFM images, XRD patterns, comparison of absorption and XRD to those in previous studies, FWHM of XRD peaks, electroabsorption of $PEA_2Pb_{0.25}Sn_{0.75}I_4$ and $PEA_2Pb_{0.75}Sn_{0.25}I_4$ thin films, and $PEA_2PbBr_2Cl_2$ absorption fit (PDF)

■ AUTHOR INFORMATION

Corresponding Authors

Kameron R. Hansen − *Department of Chemistry, University of Utah, Salt Lake City, Utah 84112, United States*; Email: kameron.hansen@utah.edu

Luisa Whittaker-Brooks − *Department of Chemistry, University of Utah, Salt Lake City, Utah 84112, United States*; orcid.org/0000-0002-1130-1306; Email: luisa.whittaker@utah.edu

John S. Colton − *Department of Physics and Astronomy, Brigham Young University, Provo, Utah 84602, United States*; Email: john_colton@byu.edu

Authors

Blake Romrell − *Department of Physics and Astronomy, Brigham Young University, Provo, Utah 84602, United States*

C. Emma McClure − *Department of Physics and Astronomy, Brigham Young University, Provo, Utah 84602, United States*

Michele Eggleston − *Department of Physics and Astronomy, Brigham Young University, Provo, Utah 84602, United States*

Alex Berzansky − *Department of Chemistry, University of Utah, Salt Lake City, Utah 84112, United States*

Jeffrey Wayjer Lin − *Department of Chemistry, University of Utah, Salt Lake City, Utah 84112, United States*

Kelsey Garden − *Department of Chemistry, University of Utah, Salt Lake City, Utah 84112, United States*; orcid.org/0000-0002-0867-0741

Complete contact information is available at: https://pubs.acs.org/10.1021/acs.jpcc.3c01294

Notes

The authors declare no competing financial interest.

■ ACKNOWLEDGMENTS

This work was supported by the U.S. Department of Energy, Office of Basic Energy Sciences, Division of Materials Sciences and Engineering under award no. DE-SC0019041. K.R.H. would like to acknowledge support from the National Science Foundation thru a Graduate Research Fellowship (grant no. 1747505). M.E. was supported by the NSF REU program, grant #2051129. C.E.M. and B.R. were supported in full or in part by the BYU Department of Physics and Astronomy and the BYU College of Physical and Mathematical Sciences. L.W.B. would also like to acknowledge the Sloan Foundation through an Alfred P. Sloan Research Fellowship in Chemistry and the Dreyfus Foundation through a Camille Dreyfus Teacher−Scholar Award.

■ REFERENCES

(1) Jacobsson, T. J.; Hultqvist, A.; García-Fernández, A.; Anand, A.; Al-Ashouri, A.; Hagfeldt, A.; Crovetto, A.; Abate, A.; Ricciardulli, A. G.; Vijayan, A.; Kulkarni, A. An open-access database and analysis tool for perovskite solar cells based on the FAIR data principles. *Nat. Energy* **2022**, *7*, 107−115.

(2) Xi, J.; Loi, M. A. The Fascinating Properties of Tin-Alloyed Halide Perovskites. *ACS Energy Lett.* **2021**, *6*, 1803−1810.

(3) Goyal, A.; McKechnie, S.; Pashov, D.; Tumas, W.; van Schilfgaarde, M.; Stevanović, V. Origin of Pronounced Nonlinear Band Gap Behavior in Lead−Tin Hybrid Perovskite Alloys. *Chem. Mater.* **2018**, *30*, 3920−3928.

(4) Galkowski, K.; Surrente, A.; Baranowski, M.; Zhao, B.; Yang, Z.; Sadhanala, A.; Mackowski, S.; Stranks, S. D.; Plochocka, P. Excitonic Properties of Low-Band-Gap Lead−Tin Halide Perovskites. *ACS Energy Lett.* **2019**, *4*, 615−621.

(5) Xi, J.; Duim, H.; Pitaro, M.; Gahlot, K.; Dong, J.; Portale, G.; Loi, M. A. Scalable, Template Driven Formation of Highly Crystalline Lead-Tin Halide Perovskite Films. *Adv. Funct. Mater.* **2021**, *31*, 2105734.

(6) Hansen, K. R.; Whittaker-Brooks, L. Finding the FAIRness in perovskite photovoltaics research. *Matter* **2022**, *5*, 2461−2464.

(7) Hoke, E. T.; Slotcavage, D. J.; Dohner, E. R.; Bowring, A. R.; Karunadasa, H. I.; McGehee, M. D. Reversible photo-induced trap formation in mixed-halide hybrid perovskites for photovoltaics. *Chem. Sci.* **2015**, *6*, 613−617.

(8) Barker, A. J.; Sadhanala, A.; Deschler, F.; Gandini, M.; Senanayak, S. P.; Pearce, P. M.; Mosconi, E.; Pearson, A. J.; Wu, Y.; Srimath Kandada, A. R.; et al. Defect-Assisted Photoinduced Halide Segregation in Mixed-Halide Perovskite Thin Films. *ACS Energy Lett.* **2017**, *2*, 1416−1424.

(9) Cho, J.; Mathew, P. S.; DuBose, J. T.; Kamat, P. V. Photoinduced halide segregation in Ruddlesden−Popper 2D mixed halide perovskite films. *Adv. Mater.* **2021**, *33*, 2105585.

(10) Tang, M.-C.; Dang, H. X.; Lee, S.; Barrit, D.; Munir, R.; Wang, K.; Li, R.; Smilgies, D.-M.; De Wolf, S.; Kim, D.-Y.; et al. Wide and Tunable Bandgap MAPbBr3−xClx Hybrid Perovskites with Enhanced Phase Stability: In Situ Investigation and Photovoltaic Devices. *Solar RRL* **2021**, *5*, 2000718.

(11) Hao, F.; Stoumpos, C. C.; Chang, R. P. H.; Kanatzidis, M. G. Anomalous Band Gap Behavior in Mixed Sn and Pb Perovskites Enables Broadening of Absorption Spectrum in Solar Cells. *J. Am. Chem. Soc.* **2014**, *136*, 8094−8099.

(12) Flannery, L.; Hansen, K. R.; Ogle, J.; Powell, D.; Garden, K.; Whittaker-Brooks, L. Voltage Bias Stress Effects and Electronic Stability of π-Conjugated Crosslinked Tin Halide Perovskites. *ACS Applied Energy Materials* **2022**, *5*, 14720−14731.

(13) Hu, Z.; Lin, Z.; Su, J.; Zhang, J.; Chang, J.; Hao, Y. A review on energy band-gap engineering for perovskite photovoltaics. *Solar RRL* **2019**, *3*, 1900304.

(14) Vashishtha, P.; Ng, M.; Shivarudraiah, S. B.; Halpert, J. E. High Efficiency Blue and Green Light-Emitting Diodes Using Ruddlesden−Popper Inorganic Mixed Halide Perovskites with Butylammonium Interlayers. *Chem. Mater.* **2019**, *31*, 83−89.

(15) Zhou, Y.; Zhou, Z.; Chen, M.; Zong, Y.; Huang, J.; Pang, S.; Padture, N. P. Doping and alloying for improved perovskite solar cells. *J. Mater. Chem. A* **2016**, *4*, 17623−17635.

(16) Liu, F.; Wang, F.; Hansen, K. R.; Zhu, X. Y. Bimodal Bandgaps in Mixed Cesium Methylammonium Lead Bromide Perovskite Single Crystals. *J. Phys. Chem. C* **2019**, *123*, 14865−14870.

(17) Jiang, Q.; Tong, J.; Scheidt, R. A.; Wang, X.; Louks, A. E.; Xian, Y.; Tirawat, R.; Palmstrom, A. F.; Hautzinger, M. P.; Harvey, S. P.; et al. Compositional texture engineering for highly stable wide-bandgap perovskite solar cells. *Science* **2022**, *378*, 1295−1300.

(18) Blancon, J.-C.; Even, J.; Stoumpos, C. C.; Kanatzidis, M. G.; Mohite, A. D. Semiconductor physics of organic−inorganic 2D halide perovskites. *Nat. Nanotechnol.* **2020**, *15*, 969−985.

(19) Powell, D.; Hansen, K. R.; Flannery, L.; Whittaker-Brooks, L. Traversing Excitonic and Ionic Landscapes: Reduced-Dimensionality-Inspired Design of Organometal Halide Semiconductors for Energy Applications. *Acc. Chem. Res.* **2021**, *54*, 4371−4382.

(20) Mauck, C. M.; Tisdale, W. A. Excitons in 2D Organic−Inorganic Halide Perovskites. *Trends Chem.* **2019**, *1*, 380−393.

(21) Katan, C.; Mercier, N.; Even, J. Quantum and dielectric confinement effects in lower-dimensional hybrid perovskite semiconductors. *Chem. Rev.* **2019**, *119*, 3140−3192.

(22) Lan, C.; Zhou, Z.; Wei, R.; Ho, J. C. Two-dimensional perovskite materials: From synthesis to energy-related applications. *Materials Today Energy* **2019**, *11*, 61−82.

(23) Chen, Y.; Sun, Y.; Peng, J.; Tang, J.; Zheng, K.; Liang, Z. 2D Ruddlesden−Popper perovskites for optoelectronics. *Adv. Mater.* **2018**, *30*, 1703487.

(24) Pham, M. T.; Amerling, E.; Ngo, T. A.; Luong, H. M.; Hansen, K. R.; Pham, H. T.; Vu, T. N.; Tran, H.; Whittaker-Brooks, L.; Nguyen, T. D. Strong Rashba-Dresselhaus Effect in Nonchiral 2D Ruddlesden-Popper Perovskites. *Adv. Opt. Mater.* **2022**, *10*, 2101232.

(25) Lanzetta, L.; Marin-Beloqui, J. M.; Sanchez-Molina, I.; Ding, D.; Haque, S. A. Two-Dimensional Organic Tin Halide Perovskites with Tunable Visible Emission and Their Use in Light-Emitting Devices. *ACS Energy Lett.* **2017**, *2*, 1662−1668.

(26) Wright, N. E.; Qin, X.; Xu, J.; Kelly, L. L.; Harvey, S. P.; Toney, M. F.; Blum, V.; Stiff-Roberts, A. D. Influence of Annealing and Composition on the Crystal Structure of Mixed-Halide, Ruddlesden−Popper Perovskites. *Chem. Mater.* **2022**, *34*, 3109−3122.

(27) Li, T.; Chen, X.; Wang, X.; Lu, H.; Yan, Y.; Beard, M. C.; Mitzi, D. B. Origin of Broad-Band Emission and Impact of Structural Dimensionality in Tin-Alloyed Ruddlesden−Popper Hybrid Lead Iodide Perovskites. *ACS Energy Lett.* **2020**, *5*, 347−352.

(28) Ramirez, D.; Schutt, K.; Wang, Z.; Pearson, A. J.; Ruggeri, E.; Snaith, H. J.; Stranks, S. D.; Jaramillo, F. Layered Mixed Tin−Lead Hybrid Perovskite Solar Cells with High Stability. *ACS Energy Lett.* **2018**, *3*, 2246−2251.

(29) Chung, Y.; Kim, D. H.; Do, J. J.; Jung, J. W. *Acute Halide Control in Ruddlesden-Popper Lead-Tin Mixed Perovskite for Efficienct Perovskite Solar Cells with 1-Year Durability in Ambient Conditions*. SSRN: 2022.

(30) Ke, W.; Chen, C.; Spanopoulos, I.; Mao, L.; Hadar, I.; Li, X.; Hoffman, J. M.; Song, Z.; Yan, Y.; Kanatzidis, M. G. Narrow-Bandgap Mixed Lead/Tin-Based 2D Dion−Jacobson Perovskites Boost the Performance of Solar Cells. *J. Am. Chem. Soc.* **2020**, *142*, 15049−15057.

(31) Ovčar, J.; Leung, T. L.; Grisanti, L.; Skoko, Ž.; Vrankić, M.; Low, K.-H.; Wang, S.; You, P.-Y.; Ahn, H.; Lončarić, I.; et al. Mixed Halide Ordering as a Tool for the Stabilization of Ruddlesden−Popper Structures. *Chem. Mater.* **2022**, *34*, 4286−4297.

(32) Underwood, C. C. L.; Carey, J. D.; Silva, S. R. P. Nonlinear Band Gap Dependence of Mixed Pb−Sn 2D Ruddlesden−Popper PEA2Pb1−xSnxI4 Perovskites. *J. Phys. Chem. Lett.* **2021**, *12*, 1501−1506.

(33) Liess, M.; Jeglinski, S.; Vardeny, Z. V.; Ozaki, M.; Yoshino, K.; Ding, Y.; Barton, T. Electroabsorption spectroscopy of luminescent and nonluminescent π-conjugated polymers. *Phys. Rev. B* **1997**, *56*, 15712.

(34) Hansen, K. R.; McClure, C. E.; Colton, J. S.; Whittaker-Brooks, L. Franz-Keldysh and Stark Effects in Two-Dimensional Metal Halide Perovskites. *PRX Energy* **2022**, *1*, No. 013001.

(35) Jeglinski, S. A. *Electroabsorption spectroscopy of conjugated polymers and carbon fullerenes and conjugated-polymer light-emitting devices*. The University of Utah, 1996.

(36) Shibuya, K.; Koshimizu, M.; Nishikido, F.; Saito, H.; Kishimoto, S. Poly [bis (phenethylammonium)[dibromidoplumbate (II)]-di-μ-bromido]. *Acta Crystallogr., Sect. E: Struct. Rep. Online* **2009**, *65*, m1323−m1324.

(37) Menahem, M.; Dai, Z.; Aharon, S.; Sharma, R.; Asher, M.; Diskin-Posner, Y.; Korobko, R.; Rappe, A. M.; Yaffe, O. Strongly Anharmonic Octahedral Tilting in Two-Dimensional Hybrid Halide Perovskites. *ACS Nano* **2021**, *15*, 10153−10162.

(38) Cao, D. H.; Stoumpos, C. C.; Yokoyama, T.; Logsdon, J. L.; Song, T.-B.; Farha, O. K.; Wasielewski, M. R.; Hupp, J. T.; Kanatzidis, M. G. Thin Films and Solar Cells Based on Semiconducting Two-Dimensional Ruddlesden−Popper $(CH_3(CH_2)_3NH_3)_2(CH_3NH_3)_{n-1}Sn_nI_{3n+1}$ Perovskites. *ACS Energy Lett.* **2017**, *2*, 982−990.

(39) Slater, J. C. Atomic radii in crystals. *The Journal of Chemical Physics* **1964**, *41*, 3199−3204.

(40) Braun, M.; Frey, W. Crystal structure of bis (2-phenylethylammonium) lead tetrachloride, C16H24Cl4N2Pb. *Zeitschrift für Kristallographie-New Crystal Structures* **1999**, *214*, 337−338.

(41) Kumawat, N. K.; Tripathi, M. N.; Waghmare, U.; Kabra, D. Structural, Optical, and Electronic Properties of Wide Bandgap Perovskites: Experimental and Theoretical Investigations. *J. Phys. Chem. A* **2016**, *120*, 3917−3923.

(42) Pistor, P.; Burwig, T.; Brzuska, C.; Weber, B.; Fränzel, W. Thermal stability and miscibility of co-evaporated methyl ammonium lead halide (MAPbX 3, X= I, Br, Cl) thin films analysed by in situ X-ray diffraction. *J. Mater. Chem. A* **2018**, *6*, 11496−11506.

(43) Aspnes, D. E. Third-derivative modulation spectroscopy with low-field electroreflectance. *Surf. Sci.* **1973**, *37*, 418−442.

(44) Hansen, K. R.; McClure, C. E.; Powell, D.; Hsieh, H. C.; Flannery, L.; Garden, K.; Miller, E. J.; King, D. J.; Sainio, S.; Nordlund, D.; Colton, J. S.; Whittaker-Brooks, L. Low Exciton Binding Energies and Localized Exciton−Polaron States in 2D Tin Halide Perovskites. *Adv. Opt. Mater.* **2022**, 2102698.

(45) Amerling, E.; Hansen, K. R.; Whittaker-Brooks, L. Resolving buried optoelectronic features in metal halide perovskites via modulation spectroscopy studies. *J. Mater. Chem. A* **2021**, *9*, 23746−23764.

(46) Hansen, K. R.; Wong, C. Y.; McClure, C. E.; Romrell, B.; Flannery, L.; Powell, D.; Garden, K.; Berzansky, A.; Eggleston, M.; King, D. J.; et al. Uncovering Unique Screening Effects in 2D Perovskites: Implications for Exciton and Band Gap Engineering. *PREPRINT (Version 1) available at Research Square* **2023**, [DOI: 10.21203/rs.3.rs-2667143/v1]

(47) Thouin, F.; Valverde-Chávez, D. A.; Quarti, C.; Cortecchia, D.; Bargigia, I.; Beljonne, D.; Petrozza, A.; Silva, C.; Srimath Kandada, A. R. Phonon coherences reveal the polaronic character of excitons in two-dimensional lead halide perovskites. *Nat. Mater.* **2019**, *18*, 349−356.

(48) Kahmann, S.; Duim, H.; Fang, H.-H.; Dyksik, M.; Adjokatse, S.; Medina, M. R.; Pitaro, M.; Plochocka, P.; Loi, M. A. Photophysics of Two-Dimensional Perovskites: Learning from Metal Halide Substitution. *Adv. Funct. Mater.* **2021**, *31*, 2103778.

(49) Jiang, Z.; Liu, Z.; Li, Y.; Duan, W. Scaling universality between band gap and exciton binding energy of two-dimensional semiconductors. *Phys. Rev. Lett.* **2017**, *118*, No. 266401.

(50) Lanzani, G. *The photophysics behind photovoltaics and photonics*; Wiley-VCH 2012.

(51) Wang, F.; Shan, J.; Islam, M. A.; Herman, I. P.; Bonn, M.; Heinz, T. F. Exciton polarizability in semiconductor nanocrystals. *Nat. Mater.* **2006**, *5*, 861−864.

(52) Horvath, A.; Weiser, G.; Baker, G. L.; Etemad, S. Influence of disorder on the field-modulated spectra of polydiacetylene films. *Phys. Rev. B* **1995**, *51*, 2751−2758.

(53) Dow, J. D. Effects of final-state interactions on modulation spectra of semiconductors. *Surf. Sci.* **1973**, *37*, 787−803.

(54) Ouhbi, H.; Ambrosio, F.; De Angelis, F.; Wiktor, J. Strong Electron Localization in Tin Halide Perovskites. *J. Phys. Chem. Lett.* **2021**, *12*, 5339−5343.

(55) Zhang, Y.; Liu, Y.; Xu, Z.; Ye, H.; Li, Q.; Hu, M.; Yang, Z.; Liu, S. Two-dimensional (PEA)2PbBr4 perovskite single crystals for a high performance UV-detector. *J. Mater. Chem. C* **2019**, *7*, 1584−1591.

(56) Zhang, Y.; Liu, Y.; Xu, Z.; Yang, Z.; Liu, S. 2D Perovskite Single Crystals with Suppressed Ion Migration for High-Performance Planar-Type Photodetectors. *Small* **2020**, *16*, 2003145.